PAPER

Check for updates

Improved pseudocapacitive charge storage in highly ordered mesoporous TiO₂/carbon nanocomposites as high-performance Li-ion hybrid supercapacitor anodes†

Yujin Lee,[a] Seoa Kim,[a] Jeong Han Lee,[b] Kwang Chul Roh, [iD][b] Eunho Lim [iD] *[c] and Jinwoo Lee [iD] *[a]

A Li-ion hybrid supercapacitor (Li-HSCs), an integrated system of a Li-ion battery and a supercapacitor, is an important energy-storage device because of its outstanding energy and power as well as long-term cycle life. In this work, we propose an attractive material (a mesoporous anatase titanium dioxide/carbon hybrid material, m-TiO₂-C) as a rapid and stable Li⁺ storage anode material for Li-HSCs. m-TiO₂-C exhibits high specific capacity ($\sim$198 mA h g^{-1} at 0.05 A g^{-1}) and promising rate performance ($\sim$90 mA h g^{-1} at 5 A g^{-1}) with stable cyclability, resulting from the well-designed porous structure with nanocrystalline anatase TiO₂ and conductive carbon. Thereby, it is demonstrated that a Li-HSC system using a m-TiO₂-C anode provides high energy and power ($\sim$63 W h kg^{-1}, and $\sim$4044 W kg^{-1}).

Introduction

High-power energy-storage devices have been regarded as indispensable systems for medium- and large-scale energy-storage applications such as electric vehicles (EVs) and smart grid technologies. This is because the medium- and large-scale energy storage applications require fast charging and discharging behaviors with long cycle lifetime.[1,2] An electric double-layer capacitor (EDLC), which is one of the typical supercapacitors, is the representative energy-storage device that provides highly excellent power abilities (2–5 kW kg^{-1}) with stable cyclability.[3–6] However, in spite of its superb abilities, it suffers from low energy performance ($\sim$10 W h kg^{-1}) due to its charge-storage mechanism being based on the physisorption of solvated ions at electrode/electrolyte interfaces.[7–9]

As its alternative device, Li-ion hybrid supercapacitors (Li-HSCs) composed of Li-ion battery (LIB) electrode materials as anodes and EDLC electrode materials as cathodes in a non-aqueous electrolyte containing a Li salt have been intensively researched and developed in recent years.[10–12] This is because that their electrochemical performance delivering both high

energy and power abilities with stable cyclability is highly attractive. Such unique characteristics result from asymmetric charge-storage mechanisms that Li⁺ from the electrolyte inserts to the anode materials (faradaic reaction) and anions such as PF₆⁻ and ClO₄⁻ are physically adsorbed on the surface of the cathode materials (non-faradaic reaction) during the charge process.[10] However, because of the different charge-storage mechanisms between two electrodes, a kinetics imbalance issue is one of the major problems in Li-HSCs, which is should be solved to develop high-performance Li-HSCs.[13,14] In other words, the reaction mechanism of the anode materials using ionic diffusion in a crystal framework of electrode materials is much more sluggish than that of cathode materials.[15,16]

To address this kinetics issue, two kinds of strategies have intensively been considered. One of the effective strategies is to reduce particle size of electrode materials in the nanoscale regime.[15] Well-nanosized electrode materials have a variety of merits such as shortened lengths for Li⁺ diffusion/electron mobility (high-power ability) and enhanced electrode/electrolyte interface area (high capacity).[17–19] In addition, reducing particle size of electrode materials in the nanoscale leads to improved pseudocapacitive reactions associated with surface-controlled reactions, which is kinetically not limited by diffusion-controlled reactions.[20] Another strategy is to use attractive carbonaceous and Ti-based anode materials such as graphite and titanium dioxide (TiO₂).[21–24] Particularly, anatase TiO₂ is one of the promising anode materials for Li-HSCs, because of its beneficial Li⁺ insertion/extraction behaviors and a variety of merits. Firstly, it provides theoretical capacity of $\sim$168 mA h g^{-1} in the potential range of $\sim$1.7 V (*vs.* Li/Li⁺) with

[a]Department of Chemical and Biomolecular Engineering, Korea Advanced Institute of Science Technology (KAIST), Daejeon 34141, Republic of Korea. E-mail: jwlee1@kaist.ac.kr

[b]Energy and Environmental Division, Korea Institute of Ceramic Engineering and Technology (KICET), Jinju, Gyeongnam 52851, Republic of Korea

[c]Carbon Resources Institute, Korea Research Institute of Chemical Technology (KRICT), Daejeon 34114, Republic of Korea. E-mail: eunholim@krict.re.kr

† Electronic supplementary information (ESI) available. See DOI: 10.1039/c9ra07157a

small volume change (<4%) during cycling.[21,25] Therefore, compared to the graphite anode working in the potential range of ~0.2 V (vs. Li/Li⁺), it is free from Li-plating problem and can provide highly stable cycle performance.[26,27] Secondly, Li-HSCs using anatase TiO_2 anodes can use a cost-attractive and light-weight Al current collector in the anodic part instead of Cu current collector because alloying reaction between Li⁺ and Al does not take place in the potential range of 1.0–3.0 V (vs. Li/Li⁺) for anatase TiO_2. In addition, it is non-toxic and one of the highly abundant materials.[28,29] However, the drawback of anatase TiO_2 is its poor electrical conductivity and relatively low Li⁺ diffusion rate.[28,30,31]

Here, to rationally design the anatase TiO_2 as anode materials for Li-HSCs, we synthesized mesoporous anatase TiO_2/carbon nanocomposite (denote as m-TiO_2-C) by using block copolymer assisted simple synthesis method. It is clearly demonstrated in this work that design of the synthesized mesoporous electrode material comprising both nanocrystalline anatase TiO_2 and conductive carbon is highly appropriate to solve drawback of the anatase TiO_2 and to maximize its electrochemical performance (high capacity and rate capability), which result from improved Li⁺ diffusion kinetics with rapid electron transport. Furthermore, we proved that the well-designed m-TiO_2-C is highly attractive as anode materials for Li-HSCs delivering high energy and power.

Experimental

Synthesis of m-TiO_2-C

0.15 g of PEO-b-PS (poly(ethylene oxide)-b-poly(styrene), M_n = 27 466 g mol⁻¹) was dissolved in 4 mL tetrahydrofuran (THF). 0.9 mL of titanium isopropoxide (TTIP) with 0.3 mL of 35–37% hydrochloric acid (concentrated HCl) was added dropwise to the block copolymer/THF mixture solution with continuous stirring. After 1 h of stirring, the mixture solution was poured to the glass Petri dish. The solvent was evaporated overnight at 40 °C, and then dried at 100 °C. The as-synthesized transparent film was obtained and then, the collected power was heat-treated in Ar atmosphere at 700 °C for 2 h. Commercial TiO_2 purchased from Sigma Aldrich was employed for control group (denoted as com-TiO_2).

Materials characterization

Structure and chemical characterization. The structure and morphology of prepared samples were investigated using scanning electron microscopy (SEM; S-4200 field-emission, Hitachi) and high resolution-transmission electron microscopy (HR-TEM; JEOL JEM-2010). Nitrogen adsorption–desorption analysis was conducted with 77 K with Micromeritics Tristar II 3020 system to estimate pore size and specific surface area. To confirm the specific pore morphology, small-angle X-ray scattering (SAXS) patterns was detected using 4C SAXS beamlines at the Pohang Light Source (PLS). To investigate crystalline phase, X-ray diffraction (XRD) pattern was identified by D/max-2500 a diffractometer (Rigaku, Cu-Kα radiation). The carbon content of m-TiO_2-C was estimated using

thermogravimetric analysis (TGA; NETZSCH STA 449C). Electron energy loss spectroscopy (EELS) analysis was performed to identify containing elements using energy-filtering transmission electron microscopy (EF-TEM, JM-220FS).

Electrochemical measurements. For half and full-cell electrochemical tests, active materials including m-TiO_2-C and com-TiO_2 (80 wt%) were homogeneously mixed with super-P carbon (10 wt%) and polyvinyledene fluoride (PVDF, 10 wt%) in N-methyl-2-pyrrolidone (NMP). The slurries were pasted on current collector using doctor blade. The prepared electrodes were dried at 60 °C for 6 h and then, 110 °C for 12 h in vacuum oven. Subsequently, the electrodes were roll-pressed. For half-cell test, 2032-type coin cells were fabricated with lithium metal as both counter and reference electrodes in Ar-filled glovebox. The mass loading of active materials used as anode materials were carefully controlled around 1.0 mg cm⁻². The electrolyte was 1.0 M of $LiPF_6$ in mixture of ethylene carbonate/dimethyl carbonate (EC/DMC, 1 : 1 volume ratio, Panaxetec. Co., Korea). The activated carbon electrode used as cathode materials was prepared using commercially available MSP-20 (90 wt%), conductive carbon (5 wt%), and polytetrafluoroethylene (PTFE, 5 wt%). In the half-cell tests, the working voltages for anode and cathode materials were 1.0–3.0 and 3.0–4.5 V (vs. Li/Li⁺), respectively. In the case of full-cell, Li-HSC was assembled using m-TiO_2-C as an anode and MSP-20 as a cathode and the weight ratio of anode and cathode active materials was controlled to 1 : 3.5 in working voltages of 0–3.0 V. The energy and power of the Li-HSCs was calculated by numerically integrating the galvanostatic discharge profiles using eqn (1) and (2) as follows.[32]

$$E = \int_{t_1}^{t_2} IV \, dt \tag{1}$$

where I is the constant current (A g⁻¹), V is the working voltage (V), t_1 and t_2 are the start/end of discharge time (s) of Li-HSCs, respectively, and

$$P = \frac{E}{t} \tag{2}$$

where t is the discharge time (s). All electrochemical tests were conducted using the WBCS-3000 battery cycler (WonA Tech, Korea).

Results and discussion

Material characterization

The m-TiO_2-C was synthesized using a block copolymer-assisted synthesis method and schematic representation on the synthesis method is shown in Fig. 1. In brief, the Ti precursor (TTIP) and laboratory-made amphiphilic block copolymer (poly(ethylene oxide)-b-poly(styrene), PEO-b-PS) synthesized by atomic transfer radical polymerization (ATRP) were dissolved in tetrahydrofuran (THF). And then, to induce sol–gel reaction of TTIP, concentrated hydrochloric acid (HCl) was slowly added to the TTIP/block copolymer/THF mixture solution. The titanium oxide sol made by hydrolysis selectively interacts with the hydrophilic PEO part of PEO-b-PS via hydrogen bonds. During
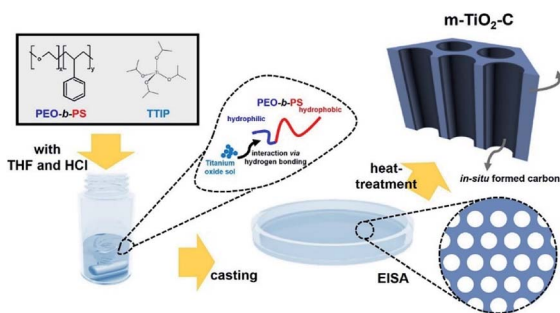
Fig. 1 Schematic illustration of the synthesis of m-TiO₂-C.

the evaporation of organic solvent at 40 °C (evaporation-induced self-assembly, ESIA), highly ordered mesostructure is formed by self-organization of titanium oxide sol/block copolymer mixture.[33–36] After drying at 100 °C to induce the cross-linkage of titanium oxide sol, the as-synthesized TiO_2/block copolymer composite was heat-treated at 700 °C under inert atmosphere (Ar condition). During heat-treatment, as-synthesized TiO_2 is converted to crystalline TiO_2. In addition, PS part of PEO-*b*-PS is converted to mechanically stable and conductive carbon (*in situ* formed carbon in m-TiO₂-C). For comparison, commercially available TiO_2 (com-TiO₂) was employed.

Fig. 2a and b show that X-ray diffraction (XRD) patterns of m-TiO₂-C and com-TiO₂ are in good agreement with anatase TiO_2 (JCPDS no. 21-1272) with no noticeable impurities. Their average crystallite sizes calculated using the Debye–Scherrer equation were ~14 (m-TiO₂-C) and ~100 (com-TiO₂) nm, respectively.[37] In addition, high-resolution transmission electron microscopy (HR-TEM, Fig. 2c) image of m-TiO₂-C clearly shows the lattice fringes of anatase TiO_2 with (101) and (004) spacing of 0.353 and 0.238 nm, respectively, again indicating

that the crystal structure of m-TiO₂-C well match the anatase TiO_2 phase. Mesoporous structure of m-TiO₂-C is identified through scanning electron microscopy (SEM) image, N_2 adsorption–desorption technique, and small-angle X-ray scattering (SAXS) patterns. SEM image (Fig. 2d) shows highly ordered mesoporous structure with uniform pore size. Compared to m-TiO₂-C, com-TiO₂ has irregular and larger particle shape/size without porosity (Fig. S1†). In addition, N_2 adsorption isotherm (Fig. 3a) of m-TiO₂-C corresponds to type IV curve with a sharp adsorption at ~0.9 P/P_0, indicating that uniform mesopores are predominant. The main pore size calculated using the Barret–Joyner–Halenda (BJH) method and specific surface area calculated using the Brunauer–Emmett–Teller (BET) of m-TiO₂-C were ~13 nm and ~123 m² g⁻¹ (Fig. 3b), respectively, which is significantly higher than that of com-TiO₂ (<2 m² g⁻¹). The mesoporous structural characterization of m-TiO₂-C is further demonstrated by SAXS pattern (Fig. 3c). Scattering peaks of m-TiO₂-C with a peak position ratio of $1 : 3^{1/2} : 4^{1/2}$ suggest that hexagonally ordered TiO_2 structure with a long-range order is well established.[38] To confirm the presence of *in situ* formed carbon in m-TiO₂-C, thermogravimetric analysis (TGA) and electron energy loss spectroscopy (EELS) analysis were employed. TGA result (Fig. 3d) proves that the *in situ* formed carbon content in the m-TiO₂-C is around 10 wt%. Furthermore, EELS analysis image (Fig. 4) directly shows the existence of *in situ* formed carbon in the m-TiO₂-C, representing that Ti, O, and C are uniformly dispersed.

Electrochemistry

Galvanostatic charge–discharge (de-lithiation and lithiation) test on m-TiO₂-C was conducted in the potential range of 1.0–3.0 V (*vs.* Li/Li⁺), showing that the m-TiO₂-C provides reversible charge capacity of ~198 mA h g⁻¹ at current of 0.05 A g⁻¹ (Fig. 5a). The typical plateau at a potential of ~1.7 V (*vs.* Li/Li⁺) demonstrates reversible Li⁺ intercalation into anatase TiO_2
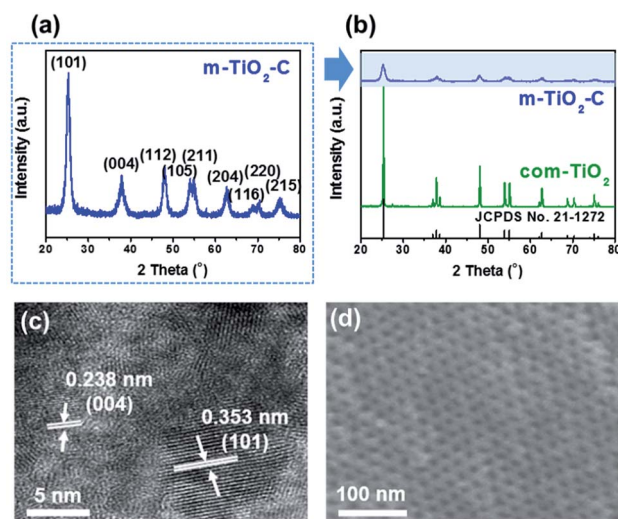

Fig. 2 (a) XRD pattern on m-TiO₂-C. (b) Comparison of XRD patterns on m-TiO₂-C and com-TiO₂. (c) HR-TEM image of m-TiO₂-C. (d) SEM image of m-TiO₂-C.
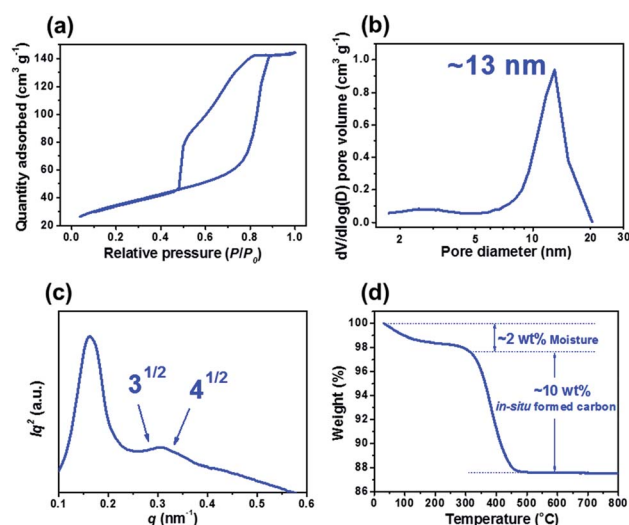

Fig. 3 (a) N_2 physisorption isotherm and (b) pore size distribution of m-TiO₂-C. (c) SAXS pattern of m-TiO₂-C. (d) TGA result of m-TiO₂-C.
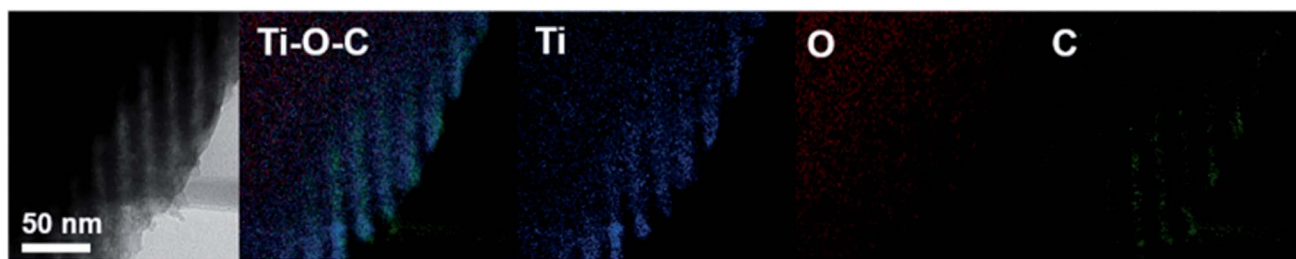
Fig. 4 EELS mapping images of m-TiO$_2$-C.

lattice, where $TiO_2 + xLi^+ + xe^- \leftrightarrow Li_xTiO_2$ $(0 \leq x \leq 0.5)$.[22,28,39] Fig. 5b shows the specific capacity of m-TiO$_2$-C is much higher ($\sim$198 mA h g^{-1}) than that of com-TiO$_2$ ($\sim$110 mA h g^{-1}) at current of 0.05 A g^{-1}. In addition, compared to com-TiO$_2$, the m-TiO$_2$-C showed much better rate capability with increasing currents from 0.05 to 5 A g^{-1}, also indicating that capacity retention of m-TiO$_2$-C with increasing currents is significantly outstanding than that of com-TiO$_2$ (Fig. S2a†). Fig. 5c and S2b† shows that the galvanostatic charge–discharge curves of m-TiO$_2$-C with increasing currents are well maintained with small overpotentials (reduced internal resistance) compared to those of com-TiO$_2$. It represents that well-ordered structure with conductive *in situ* formed carbon is highly beneficial to improve electrochemical performances of anatase TiO$_2$, mainly due to a variety of merits including (i) shortened diffusion lengths of Li$^+$, (ii) superior electron mobility, (iii) easy penetration of electrolyte, (iv) plentiful charge-storage sites, and *etc*.[34,40–42] It should be noted that the m-TiO$_2$-C exhibits better rate capability than other anatase TiO$_2$ anodes previously reported (Fig. S3†) and delivers highly stable cycle stability (capacity retention of $\sim$94% with $\sim$100% coulombic efficiency for $\sim$350 cycles) at the current of 0.5 A g^{-1} (Fig. 5d and S4†).[43–47] In addition, it shows

stable long-term cyclability at high current of 3 A g^{-1} for 1000 cycles (Fig. S4,† capacity retention of $\sim$97% with $\sim$100% coulombic efficiency). Because the excellent rate capability and long-term cycle stability are main factors for application to anodes of Li-HSCs, m-TiO$_2$-C developed in this work could be the extremely potential Li-HSC anode material.

To further reveal the reason why m-TiO$_2$-C provides superior electrochemical behaviors, we performed cyclic voltammetry (CV) tests on m-TiO$_2$-C and com-TiO$_2$ conducted at sweep rates from 0.1 to 1.0 mV s^{-1} in the potential range of 1.0–3.0 V (*vs.* Li/Li$^+$) as shown in Fig. 6a and S5.† The pair of redox peaks (1.7–2.0 V *vs.* Li/Li$^+$) of m-TiO$_2$-C and com-TiO$_2$ at sweep rate of 0.1 mV s^{-1} well match the lithiation and de-lithiation reactions. In previous studies, it is well known that the anatase TiO$_2$ is influenced by the diffusion-controlled process with a two-phase process. Therefore, from $i = av^b$ equation (where a (mV s^{-1})) with CV tests, b value of anatase TiO$_2$ is close to 0.5, indicating that the diffusion-controlled reactions is more dominant than
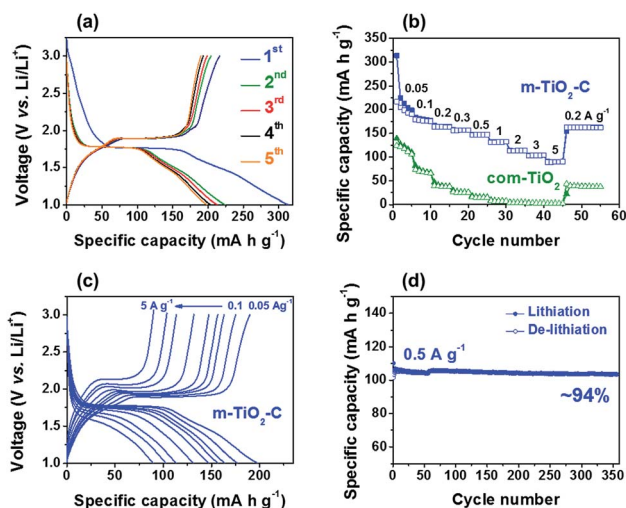

Fig. 5 (a) Galvanostatic charge–discharge profiles of m-TiO$_2$-C at 0.05 A g^{-1}. (b) Comparison of rate capability of TiO$_2$ electrodes at different currents from 0.05 to 5 A g^{-1}. (c) Galvanostatic charge–discharge profiles of m-TiO$_2$-C at various currents from 0.05 to 5 A g^{-1}. (d) Cycle performance of m-TiO$_2$-C at a current of 0.5 A g^{-1}.
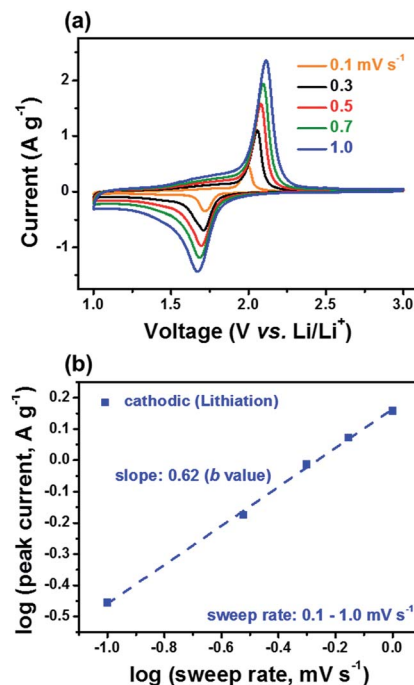

Fig. 6 (a) CV curves of m-TiO$_2$-C at different sweep rates of 0.1–1.0 mV s^{-1}. (b) log(*i*) *vs.* log(*v*) plot of cathodic peak current on m-TiO$_2$-C electrode.
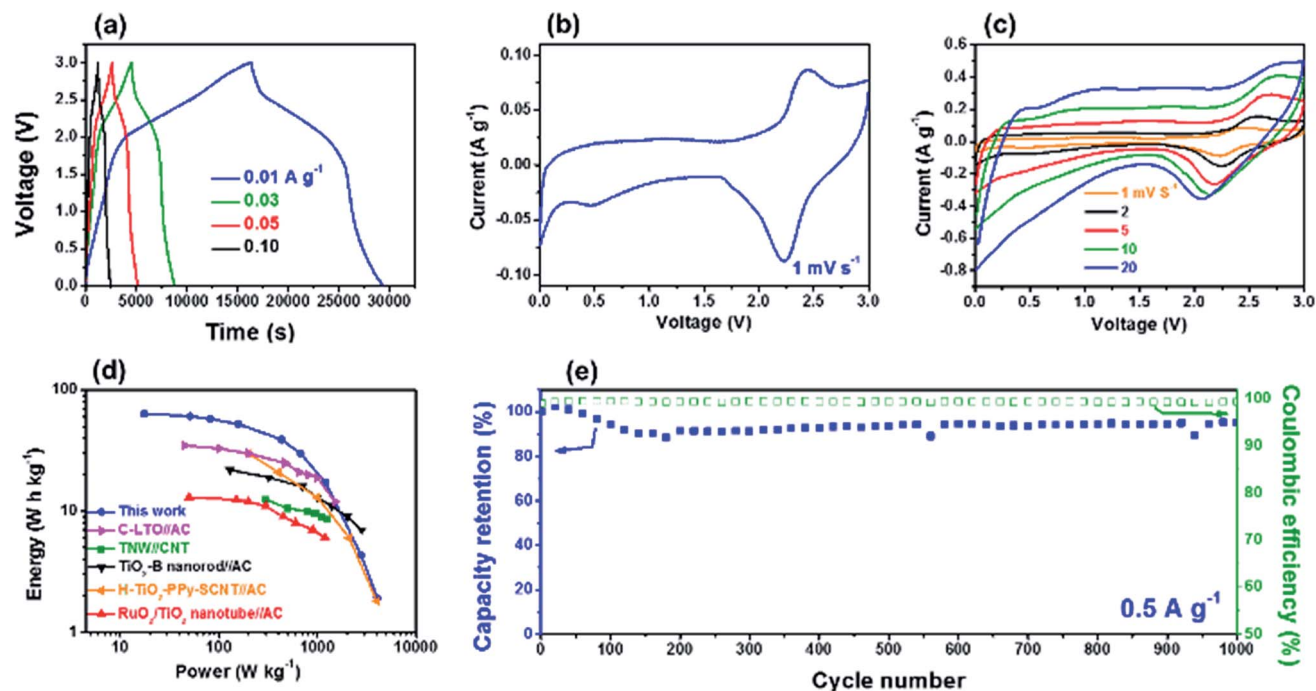
Fig. 7 (a) Galvanostatic charge–discharge profiles of the Li-HSC at different currents from 0.01 to 0.1 A g^{-1}. (b and c) CV curves of the Li-HSCs at different sweep rates of 1–20 mV s^{-1}. (d) Ragone plots compared with previously reported results. (e) Cycle performance of the Li-HSC at a current of 0.5 A g^{-1}.

the surface-controlled reaction ($b = 1.0$).[20,48,49] As shown in Fig. 6b and S6,†b value of m-TiO$_2$-C obtained from peak currents of the lithiation process is around 0.62, indicative of that the charge-storage reaction mechanism in m-TiO$_2$-C is influenced by both the surface- and diffusion-controlled reactions (improved pseudocapacitive reaction).[49] It is considerably contrast to that of com-TiO$_2$ showing severe deviation with increasing sweep rates from 0.1 to 1.0 mV s^{-1} because of huge internal resistance. In addition, b values of m-TiO$_2$-C obtained in potential range of 1.2–2.1 V ($vs.$ Li/Li$^+$) are also higher than 0.5 (Fig. S6†).

Before building Li-HSC system using the m-TiO$_2$-C anode, electrochemical behavior of MSP-20 (commercially available activated carbon) as a cathode material for the Li-HSC was investigated by galvanostatic charge–discharge half-cell test. Fig. S7† shows that reversible specific capacity of the MSP-20 is ~60 mA h g^{-1} at a current of 0.05 A g^{-1} in the voltage range of 3.0–4.5 V ($vs.$ Li/Li$^+$). Considering the specific capacities and working voltages between m-TiO$_2$-C anode and MSP-20 cathode, the Li-HSC system using m-TiO$_2$-C anode and MSP-20 cathode was carefully assembled and its galvanostatic charge–discharge tests were conducted at various currents in the potential range of 0.0–3.0 V (Fig. 7a and S8†). Galvanostatic charge–discharge curves of Li-HSC using m-TiO$_2$-C as anode and MSP-20 as cathode at current rates from 0.01 to 5 A g^{-1} do not exhibit typical triangular shape, dissimilar to those of conventional symmetric SCs.[50] It is again confirmed from CV data at sweep rates of 1–20 mV s^{-1} (Fig. 7b and c) that the CV profile does not follows a typical rectangular shape of conventional symmetric SCs. The galvanostatic charge–discharge and CV shapes of the Li-HSC are mainly due to combination of the faradaic reaction at the m-TiO$_2$-C anode and the non-faradaic reaction at the MSP-20 cathode.[22] The maximum energy and power of the Li-HSC calculated using eqn (1) and (2) with galvanostatic charge–discharge curves were ~63 W h kg^{-1} and ~4044 W kg^{-1}, respectively. The Ragone plot on the trade of relationship between energy and combination of the faradaic reaction at the m-TiO$_2$-C anode and the non-faradaic reaction at the MSP-20 cathode.[22] The maximum energy and power of the Li-HSC calculated using eqn (1) and (2) with galvanostatic charge–discharge curves were ~63 W h kg^{-1} and ~4044 W kg^{-1}, respectively. The Ragone plot on the trade of relationship between energy and power shows that its energy and power is much better than that of other results previously reported (Fig. 7d).[43,51–54] Finally, long-term cycle stability of the Li-HSC was investigated. Fig. 7e shows that the cycling stability of the Li-HSC at a current of 0.5 A g^{-1} is well maintained with ~100% coulombic efficiency for 1000 cycles. The Ragone plot and cycle performance data imply that m-TiO$_2$-C is highly suitable as the anode material for Li-HSC system.

Conclusions

In summary, we reported the block copolymer assisted one-pot synthesis method of m-TiO$_2$-C and its application for high-power anode materials of Li-HSC. The m-TiO$_2$-C delivered high specific capacity (~198 mA h g^{-1} at 0.05 A g^{-1}) and rate capability (~90 mA h g^{-1} at 5 A g^{-1}) with stable cycle performance. Its electrochemical performance was superior compared to com-TiO$_2$, mainly due to synergistic effects of

unique mesostructure and hybridization between anatase TiO_2 and *in situ* formed carbon. Thereby, the Li-HSC system using the m-TiO_2-C anode possessed high energy and power abilities ($\sim$63 W h kg^{-1} and $\sim$4044 W kg^{-1}) in the potential range of 0.0–3.0 V, implying that the energy-storage device (Li-HSC) can be a promising alternative to conventional symmetric SCs.

Conflicts of interest

There are no conflicts to declare.

Acknowledgements

Notes and references

1 B. Kang and G. Ceder, *Nature*, 2009, **458**, 190–193.
2 M. H. Hsieh, G. A. Li, W. C. Chang and H. Y. Tuan, *J. Mater. Chem. A*, 2017, **5**, 4114–4121.
3 J. Yan, Q. Wang, T. Wei and Z. Fan, *Adv. Energy Mater.*, 2014, **4**, 1300816.
4 G. Zhang and X. W. Lou, *Adv. Mater.*, 2013, **25**, 976–979.
5 G. F. Chen, Y. Z. Su, P. Y. Kuang, Z. Q. Liu, D. Y. Chen, X. Wu, N. Li and S. Z. Qiao, *Chem. - Eur. J.*, 2015, **21**, 4614–4621.
6 S. Ghosh, S. Jeong and S. R. Polaki, *Korean J. Chem. Eng.*, 2018, **35**, 1389–1408.
7 P. Simon, Y. Gogotsi and B. Dunn, *Science*, 2014, **343**, 1210–1211.
8 D. Pech, M. Brunet, H. Durou, P. Huang, V. Mochalin, Y. Gogotsi, P. L. Taberna and P. Simon, *Nat. Nanotechnol.*, 2010, **5**, 651–654.
9 E. M. Jin, H. Lee, H. Jun and S. Jeong, *Korean J. Chem. Eng.*, 2017, **34**, 885–891.
10 K. Naoi, S. Ishimoto, J. Miyamoto and W. Naoi, *Energy Environ. Sci.*, 2012, **5**, 9363–9373.
11 C. M. Lai, T. L. Kao and H. Y. Tuan, *J. Power Sources*, 2018, **379**, 261–269.
12 R. Yi, S. Chen, J. Song, M. L. Gordin, A. Manivannan and D. Wang, *Adv. Funct. Mater.*, 2014, **24**, 7433–7439.
13 E. Lim, C. Jo, H. Kim, M. Kim, Y. Mun, Y. Ye, J. Hwang, K. Ha, K. Roh and J. Lee, *ACS Nano*, 2015, **9**, 7497–7505.
14 E. Lim, W. Lim, C. Jo, J. Chun, M. Kim, K. Roh and J. Lee, *J. Mater. Chem. A*, 2017, **5**, 20969–20977.
15 E. Lim, C. Jo and J. Lee, *Nanoscale*, 2016, **8**, 7827–7833.
16 V. Aravindan, J. Gnanaraj, Y. S. Lee and S. Madhavi, *Chem. Rev.*, 2014, **114**, 11619–11635.
17 Z. Wang, L. Zhou and X. W. Lou, *Adv. Mater.*, 2012, **24**, 1903–1911.

18 Z. Yang, D. Choi, S. Kerisit, K. M. Rosso, D. Wang, J. Zhang, G. Graff and J. Liu, *J. Power Sources*, 2009, **192**, 588–598.
19 A. K. Mondal, K. Kretschmer, Y. Zhao, H. Liu, H. Fan and G. Wang, *Microporous Mesoporous Mater.*, 2017, **246**, 72–80.
20 J. Wang, J. Polleux, J. Lim and B. Dunn, *J. Phys. Chem. C*, 2007, **40**, 14925–14931.
21 D. Deng, M. Kim, J. Y. Lee and J. Cho, *Energy Environ. Sci.*, 2009, **2**, 818–837.
22 H. Kim, M. Cho, M. Kim, K. Park, H. Gwon, Y. Lee, K. C. Roh and K. Kang, *Adv. Energy Mater.*, 2013, **3**, 1500–1506.
23 S. Ghosh, W. D. Yong, E. M. Jin, S. R. Polaki, S. Jeong and H. Jun, *Korean J. Chem. Eng.*, 2019, **36**, 312–320.
24 W. Lee, S. Jeong, H. Lee, B. Kim, K. An, Y. Park and S. Jung, *Korean J. Chem. Eng.*, 2017, **34**, 2993–2998.
25 L. Thirugunanam, S. Kaveri, V. Etacheri, S. Ramaprabhu, M. Dutta and V. G. Pol, *Mater. Charact.*, 2017, **131**, 64–71.
26 Y. Liu and Y. Yang, *J. Nanomater.*, 2016, **2016**, 1–15.
27 V. Etacheri, C. N. Hong, J. Tang and V. G. Pol, *ACS Appl. Mater. Interfaces*, 2018, **10**, 4652–4661.
28 J. Shin, D. Samuelis and J. Maier, *Adv. Funct. Mater.*, 2011, **21**, 3464–3472.
29 Y. Guan, T. Hu, J. Wu, L. Zhao, F. Tian, W. Pan, P. He, W. Qi, F. Li and K. Xu, *Korean J. Chem. Eng.*, 2019, **36**, 115–125.
30 Y. Qiu, K. Yan, S. Yang, L. Jin, H. Deng and W. Li, *ACS Nano*, 2010, **4**, 6515–6526.
31 J. S. Chen, H. Liu, S. Z. Qiao and X. W. Lou, *J. Mater. Chem.*, 2011, **21**, 5687–5692.
32 F. Zhang, T. Zhang, X. Yang, L. Zhang, K. Leng, Y. Huang and Y. Chen, *Energy Environ. Sci.*, 2013, **6**, 1623.
33 J. Hwang, C. Jo, M. Kim, J. Chun, E. Lim, S. Kim, S. Jeong, Y. Kim and J. Lee, *ACS Nano*, 2015, **9**, 5299–5309.
34 C. Jo, Y. Kim, J. Hwang, J. Shim, J. Chun and J. Lee, *Chem. Mater.*, 2014, **26**, 3508–3514.
35 J. Lee, M. C. Orilall, S. C. Warren, M. Kamperman, F. J. DiSalvo and U. Wiesner, *Nat. Mater.*, 2008, **7**, 222–228.
36 J. Hwang, J. Kim, E. Ramasamy, W. Choi and J. Lee, *Microporous Mesoporous Mater.*, 2011, **143**, 149–156.
37 A. D. Krawitz, *Introduction to Diffraction in Materials Science and Engineering*, Wiley, New York, 2001, p. 168.
38 M. Templin, A. Franck, A. D. Chensne, H. Leist, Y. Zhang, R. Ulrich, V. Schadler and U. Wiesner, *Science*, 1997, **278**, 1795–1798.
39 Y. Guo, Y. Hu and J. Maier, *Chem. Commun.*, 2006, **26**, 2783–2785.
40 Y. Ye, C. Jo, I. Jeong and J. Lee, *Nanoscale*, 2013, **5**, 4584–4605.
41 C. Jo, J. Hwang, H. Song, A. H. Dao, Y. Kim, S. Lee, S. Hong, S. Yoon and J. Lee, *Adv. Funct. Mater.*, 2013, **23**, 3747–3754.
42 E. Kang, Y. Jung, G. Kim, J. Chun, U. Wiesner, A. C. Dillon, J. Kim and J. Lee, *Adv. Funct. Mater.*, 2011, **21**, 4349–4357.
43 G. Tang, L. Cao, P. Xiao, Y. Zhang and H. Liu, *J. Power Sources*, 2017, **355**, 1–7.
44 E. Lim, H. Shim, S. Fleischmann and V. Presser, *J. Mater. Chem. A*, 2018, **6**, 9480.
45 H. Wang, C. Guan, X. Wang and H. J. Fan, *Small*, 2015, **11**, 1470–1477.

46 T. Brousse, R. Marchand, P. Taberna and P. Simon, *J. Power Sources*, 2006, **158**, 571–577.

47 V. Aravindan, M. V. Reddy, S. Madnavi, S. G. Mhaisalkar, G. V. Subba Rao and B. V. R. Chowdari, *J. Power Sources*, 2011, **196**, 8850–8854.

48 V. Augustyn, J. Come, M. A. Lowe, J. W. Kim, P. L. Taberna, S. H. Tolbert, H. D. Abruna, P. Simon and B. Dunn, *Nat. Mater.*, 2013, **12**, 518–522.

49 H. Lindstrom, S. Sodergren, A. Solbrand, H. Rensmo, J. Hjelm, A. Hagfeldt and S. Lindquist, *J. Phys. Chem. B*, 1997, **101**, 7717–7722.

50 K. Karthikeyan, S. Amaresh, V. Aravindan, H. Kim, K. S. Kang and Y. S. Lee, *J. Mater. Chem. A*, 2013, **1**, 707–714.

51 H. Jung, N. Venugopal, B. Scrosati and Y. Sun, *J. Power Sources*, 2013, **221**, 266–271.

52 Q. Wang, Z. Wen and J. Li, *Adv. Funct. Mater.*, 2006, **16**, 2141–2146.

53 V. Aravindan, N. Shubha, W. Chui and S. Madhavi, *J. Mater. Chem. A*, 2013, **1**, 6145–6151.

54 Y. Wang, W. Wang and Y. Xia, *Electrochim. Acta*, 2005, **50**, 5641–5646.